processes

MDPI

Article

Dynamic Decoupled Current Control for Smooth Torque of the Open-Winding Variable Flux Reluctance Motor Using Integrated Torque Harmonic Extended State Observer

El Moundher Aouiche [1,*], Xu Liu [1,*], Abdelaziz Aouiche [2], Mustafa Alrayah Hassan [3], Mohammed Echarif Aguida [4], Junaid Ali Khan [1] and Yang Cao [1]

[1] State Key Laboratory of Reliability and Intelligence of Electrical Equipment, Hebei University of Technology, Tianjin 300130, China; engrjunaidkhan.ep@gmail.com (J.A.K.); 201911401018@stu.hebut.edu.cn (Y.C.)
[2] Faculty of Sciences and Technologies, Electrical Engineering Department, Larbi Tebessi University, Tebessa 12000, Algeria
[3] The Future Reliable Electricity & Energy System Integration Laboratory, University of Vaasa, Yliopistonranta 10, Fabriikki F238, 65200 Vaasa, Finland; mustafaa@uwasa.fi
[4] School of Electrical and Information Engineering, Tianjin University, Tianjin 300072, China; 6120000294@tju.edu.cn
* Correspondence: 201940000012@stu.hebut.edu.cn (E.M.A.); liuxu@hebut.edu.cn (X.L.)

Abstract: Variable Flux Reluctance Machines (VFRMs) face multiple interconnected challenges that limit their performance, particularly in high-performance applications such as electric vehicles (EVs), where smooth torque output and robust operation are critical. Chief among these challenges are complex inter-axis couplings, including cross-coupling in the dq-axis, differential term coupling in the d0-axis, and disturbances propagating from the 0-axis to the q-axis. Additionally, harmonic disturbances associated with torque ripple exacerbate performance issues, resulting in degraded dynamic behavior. These challenges hinder current loop controllers, preventing effective management of winding impedance voltage drops and inter-axis coupling terms without advanced decoupling strategies. To address these challenges, this paper proposes a novel integrated torque harmonic extended state observer (ITHESO) within a decoupled current control designed to ensure fast and accurate current tracking, system stability, and torque ripple reduction. The ITHESO identifies and compensates for total current disturbances, including harmonic components, through feed-forward compensation within the current loop. Furthermore, the influence of control parameters and the effects of parameter mismatches on stability, torque ripple reduction, and disturbance rejection are thoroughly analyzed. Experimental validations demonstrate that the proposed strategy significantly enhances torque dynamics and reduces torque ripple, outperforming the conventional Active Disturbance Rejection Control (ADRC), which does not explicitly address disturbances associated with torque ripple. These advancements position the VFRM with the ITHESO as a competitive option for high-performance EV propulsion systems, offering smooth operation, noise reduction, and reliable performance under varying speeds and loads.

Keywords: Variable Flux Reluctance Machines (VFRMs); current control; torque ripple

check for updates

Academic Editor: Mohan Lal Kolhe

Received: 1 December 2024
Revised: 14 January 2025
Accepted: 15 January 2025
Published: 17 January 2025

Citation: Aouiche, E.M.; Liu, X.; Aouiche, A.; Hassan, M.A.; Aguida, M.E.; Khan, J.A.; Cao, Y. Dynamic Decoupled Current Control for Smooth Torque of the Open-Winding Variable Flux Reluctance Motor Using Integrated Torque Harmonic Extended State Observer. *Processes* **2025**, *13*, 263. https://doi.org/10.3390/pr13010263

Copyright: © 2025 by the authors. Licensee MDPI, Basel, Switzerland. This article is an open access article distributed under the terms and conditions of the Creative Commons Attribution (CC BY) license (https://creativecommons.org/licenses/by/4.0/).

1. Introduction

Variable flux reluctance machines (VFRMs) represent a viable substitute for conventional induction machines due to their distinctive doubly salient architecture and uncomplicated configuration [1,2]. They exhibit enhanced efficiency by eliminating rotor losses,

possess a more straightforward design that minimizes expenses, and afford superior torque regulation across an extensive speed spectrum. With an increased torque density, VFRMs further expand their applicability to high-performance domains, such as electric vehicles (EV), where smooth torque output and minimal noise are critical for passenger comfort. To enhance performance and reliability while functioning within a constrained DC bus voltage, VFRMs are constructed to feature a DC field winding paired with an AC armature winding [2,3]. In achieving a closed circuit for the zero-sequence current (DC component), a mutual DC link is utilized alongside the open winding [4,5].

Among the most common issues in machine drives are coupling terms in dq0-axis and torque ripple, which have the potential to induce negative mechanical vibrations and auditory disturbances. Therefore, addressing torque ripple has evolved into a pivotal concern within both research endeavors and commercial applications.

In order to diminish the impacts of torque ripple, two fundamental categories of approach can be implemented [6]. The initial category encompasses motor-design strategies, which include techniques such as skewing [7], the design of the pole arcs of the stator [8], and the optimization of permanent magnet configurations [9]. These methods tend to be costly, and they are predominantly chiefly appropriate for recently designed machinery. The second category consists of active control methodologies, which are favored due to their cost-effectiveness and adaptability. Among the various active control strategies, speed control techniques that facilitate smooth speed regulation through torque compensation based on detected disturbances are garnering increasing attention across numerous applications [10]. Observer-based control strategies, such as the dual variable bandwidth extended state observers (DVB-ESOs) proposed in [11], have shown promise in enhancing the dynamic performance of machine drives. In the context of finite-control-set model predictive torque control (FCS-MPTC), DVB-ESOs are used to improve disturbance rejection and address parameter mismatches in PMSM systems.

Typically, there exist two methods for the observation of disturbances. One method involves the utilization of an integrator within the feedback control system. In cases where the reference functions as a direct signal, the establishment of a typical proportional-integral (PI) controller can secure the attainment of zero steady-state error. Conversely, in cases where the reference entails a resonant signal, it is necessary to apply a resonant controller or generalized integrator (GI) [12]. In the stationary reference frame, a resonant controller achieves a similar effect to an integrator in the synchronous reference frame, providing an effective method for harmonic suppression, albeit requiring additional frame transformations [13]. When both direct and resonant signals are present in the reference, a proportional-integral-resonant (PIR) controller is recommended [14]. For addressing multiple harmonics, multiple resonant controllers [15], a repetitive controller [16], or harmonic injection [17] can be utilized.

Although these controllers demonstrate impressive abilities to reject periodic disturbances, they simultaneously hinder tracking performance owing to their single-degree-of-freedom nature. To mitigate this issue, the use of two-degree-of-freedom (TDOF) controllers is advisable. In [18], to prevent the PIR controller from amplifying high frequency elements, a tracking differentiator is used as a prefilter to refine the velocity reference. Conversely, in [19], a partial prefilter in which the prefilter is solely used for the resonant controller is designed, while a traditional PI controller is used for constant disturbance mitigation. However, the arrangement of the partial prefilter poses considerable difficulties.

An alternative approach for the observation of disturbances involves the application of disturbance observers (DOBs), which enable the seamless achievement of TDOF control [20]. The primary objective of DOBs is to estimate disturbances by compelling the predicted output to align with the actual output of the system. Likewise, controllers employed

in feedback regulation can be applied within observers. For instance, a proportional regulator may be integrated into a DOB, while a PI regulator could be utilized in an ESO. Research indicates that various DOBs act as low-pass filters in perturbation detection [21]. Thus, general PI observers [22] may be inadequate for periodic tracking. Similarly, quasi-fractional-resonant normalized extended state observers (NESOs) have been introduced to suppress speed ripple caused by current measurement errors [23]. These methods highlight the potential of advanced observer designs in mitigating periodic disturbances and ensuring robust control.

In [24], in order to mitigate the sixth-order current harmonics resulting from the dead time effect in resonant controllers, the DOB is applied, allegedly using a dual-loop configuration. Nonetheless, the experiments are restricted to a low-speed regime, with the maximum resonant frequency capped at 60 Hz. A thorough design methodology for this particular type of DOB, along with a corresponding stability analysis, is presented in [25]. In contrast to the DOB-centric control methodology, the ADRC utilizing an ESO exhibits enhanced efficacy in mitigating measurement noise due to its ability to simultaneously observe both speed and disturbances. In [26], a GIESO is used to minimize the current harmonics induced by an imbalanced grid. This leads to a higher maximum resonance frequency of 300 Hz. However, the analysis does not consider higher frequency disturbances. It also overlooks the effects of the one-step delay induced by PWM updates. In order to improve the robustness of the system to frequency deviations, a quasi-resonant ESO is introduced in [27]. The controller is formulated in the discrete time domain, which facilitates dealing with one-step delays. Analysis shows that if the sampling interval is too large, the system may become unstable. However, high frequency disturbances are also ignored. In [28], PIR is used as current control to counteract the higher-order harmonics of the torque ripple. This eliminates the delay associated with the inner current loop. On the other hand, implementing a PIR current controller increases the complexity of the algorithm.

Reflecting on the earlier analyses, this paper unveils an innovative integrated torque harmonic extended state observer (ITHESO) incorporated within a decoupled current control schema, specifically intended to diminish torque ripple in the VFRM. The proposed ITHESO, unlike ADRC and GIESO, integrates the torque harmonic component to effectively reduce torque ripple while also addressing the inter-axis couplings present in the current loop control, thereby bypassing the complexities faced with the PIR controller. Initially, a comprehensive assessment of the current control loop is undertaken to validate that VFRMs are characterized by intricate inter-axis couplings and torque ripple. To address this challenge, the ITHESO is formulated. In this approach, the torque harmonic is treated as a periodic disturbance and integrated into each of the dq0-axis current controllers, while the validation of the system's stability is ensured through the application of principles outlined by Lyapunov's stability theory. Experimental evaluations substantiate the efficacy of the proposed decoupled current control strategy. The results reveal a notable reduction in the torque ripple of the open-winding VFRM, indicating consistent performance across both steady-state and transient operating conditions.

2. Mathematical Modeling of VFRM

In the VFRM design, the layout of the 6/4 VFRM incorporates both AC and DC components, as depicted in Figure 1a. Traditionally, the regulation of the DC segment of the VFRM was backed by an external H-bridge inverter connected to a separate DC bus voltage.

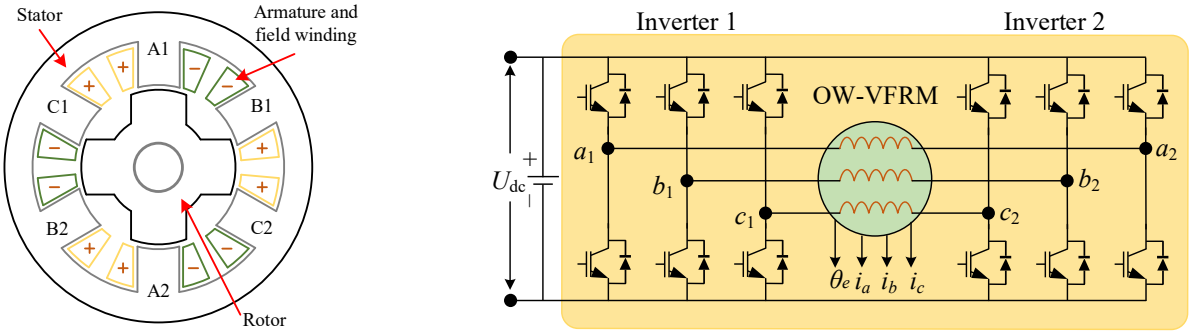

(**a**) (**b**)

Figure 1. (**a**) Integrated armature and field winding VFRM topology, (**b**) Dual inverter with Shared DC Bus.

In order to achieve maximum power output within the boundaries imposed by the DC bus voltage and to bolster system reliability, the DC and AC coils have been consolidated into a single winding. Furthermore, the open windings for both the positive and negative terminals in the VFRM are regulated through a dual inverter that employs a shared DC bus voltage, as demonstrated in Figure 1b. In this setup, the regulation of the DC component is accomplished through the zero-sequence current yielded by the dual inverter.

As stated in [29], Equation (1) for the voltage in the VFRM includes an inductance element that varies with a third harmonic order.

$$\begin{aligned}\begin{bmatrix} u_\mathrm{d} \\ u_\mathrm{q} \\ u_0 \end{bmatrix} &= R_s \begin{bmatrix} i_\mathrm{d} \\ i_\mathrm{q} \\ i_0 \end{bmatrix} + \begin{bmatrix} \frac{L_\delta}{2}\cos 3\theta_\mathrm{e} + L_\mathrm{s} & -\frac{L_\delta}{2}\sin 3\theta_\mathrm{e} & M_\delta \\ -\frac{L_\delta}{2}\sin 3\theta_\mathrm{e} & \frac{L_\delta}{2}\cos 3\theta_\mathrm{e} - L_\mathrm{s} & 0 \\ \frac{L_\delta}{2} & 0 & M_\mathrm{s} \end{bmatrix} \begin{bmatrix} \frac{\mathrm{d}i_\mathrm{d}}{\mathrm{d}t} \\ \frac{\mathrm{d}i_\mathrm{q}}{\mathrm{d}t} \\ \frac{\mathrm{d}i_0}{\mathrm{d}t} \end{bmatrix} \\ &+\omega_\mathrm{e} \begin{bmatrix} -L_\delta \sin 3\theta_\mathrm{e} & -L_\delta \cos 3\theta_\mathrm{e} - L_\mathrm{s} & 0 \\ -L_\delta \cos 3\theta_\mathrm{e} + L_\mathrm{s} & L_\delta \sin 3\theta_\mathrm{e} & M_\delta \\ 0 & 0 & 0 \end{bmatrix} \begin{bmatrix} i_\mathrm{d} \\ i_\mathrm{q} \\ i_0 \end{bmatrix}\end{aligned} \quad (1)$$

Along the dq0-axis, the elements are labeled as i_d, i_q, and i_0 for the respective current components, whereas U_d, U_q, and U_0 signify the voltage components. Additionally, ω_e and θ_e correspond to the electrical angular velocity and phase angle, respectively, while R_s represents the winding resistance and M_δ represents varying components of the mutual inductance between the field and armature windings.

The primary frequency element is characterized as L_δ, while the invariant element of the self-inductance is denoted by L_s. The waveform of the self-inductance and its harmonic properties, informed by the FEA modeling, are demonstrated in Figure 2.

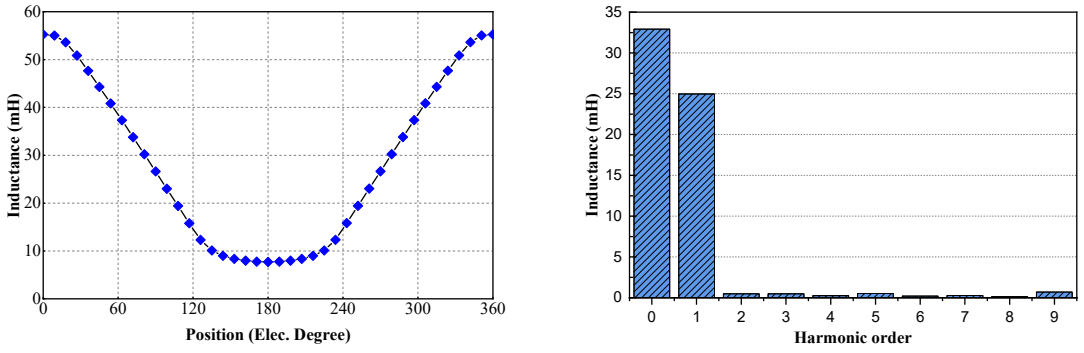

(**a**) (**b**)

Figure 2. (**a**) Waveforms of self-inductance (when i_0 = 1 A and ω_e = 400 rpm). (**b**) Harmonic content of self-inductance.

In VFRM, the self-inductance is comprised of a constant component and a harmonic linked to the primary frequency. Although the intensity of self-inductance can vary with fluctuations in the DC component, higher-order harmonics are neglected in this model, based on their minimal contribution to system dynamics. As shown in Figure 2, the amplitudes of harmonics beyond the second order are significantly smaller. Analytical studies and FEA confirm that these higher-order components have negligible influence on the torque ripple and inter-axis coupling effects. Including them would add unnecessary complexity to the model without providing meaningful improvements in accuracy. Therefore, for computational efficiency and to focus on the most critical disturbances, only the dominant harmonic components are considered in this paper.

It is also evident from Equation (1) that the self-inductance $L\delta$ varies dynamically with ωe and θe. These periodic variations significantly impact the dq0-axis voltage equations, introducing inter-axis coupling effects. These variations are significant for designing the current control strategy.

Considering ψ_{d} and ψ_{q} as the mathematical formulations of stator flux along the d-axis and q-axis, respectively, the flux within the dq-axis can be represented as follows:

$$\begin{cases} \psi_{\mathrm{d}} = L_{\mathrm{s}} i_{\mathrm{d}} + L_{\delta} i_0 \\ \psi_{\mathrm{q}} = -L_{\mathrm{s}} i_{\mathrm{q}} \end{cases} \tag{2}$$

The derivation of torque in a magneto-mechanical system can be achieved through the principle of energy conversion, utilizing an abstract circuit model that encompasses inductance, resistance, and electromotive force (EMF) elements [29]. In the case of VFRMs, the formula that illustrates the electromagnetic torque at any specific instant can be articulated as follows.

$$T_e = \frac{3}{2} N_{\mathrm{r}} \left(\psi_{\mathrm{d}} i_{\mathrm{q}} - \psi_{\mathrm{q}} i_{\mathrm{d}} \right) + \frac{3}{8} N_{\mathrm{r}} L_{\delta} \left(i_d^2 + i_q^2 \right) \sin(3\theta_e + 2\beta) \tag{3}$$

Here, N_{r} represents the number of pole pairs in the rotor, and β denotes the advanced current angle (phase shift between current and flux). It is worth noting that β influences the phase of torque ripple. Proper control of β can minimize ripple by aligning the currents with the optimal torque-producing flux vector.

The instantaneous torque of VFRM, as detailed in (3), encompasses both the average torque and the torque related to the third harmonic. The average torque is primarily derived from the interaction between the flux linkage along the dq-axis and the AC component, along with the zero-sequence element.

It is significant to emphasize that the previously mentioned model is formulated under the assumption of disregarding self-inductance saturation.

3. Current Decoupling Control Based on ITHESO for Torque Ripple Reduction

3.1. Torque Ripple Factor in the VFRM

In VFRM, the position-dependent torque ripple does not necessarily stay aligned with the sine ($3\theta_{\mathrm{e}}$) term alone. Due to mechanical or magnetic phase shifts introduced by factors such as rotor geometry, magnetic saturation, or misalignment, it is often observed that the torque ripple has both sine and cosine components.

Consider a phase-shifted version of the torque ripple. A sine function can be represented as a combination of a sine and cosine function using a phase shift according to Euler's formula

$$e^{j\phi} = \cos(\phi) + \sin(\phi) \tag{4}$$

Thus, for any angle α:

$$\begin{aligned} \sin(\alpha) &= \frac{e^{j\alpha}-e^{-j\alpha}}{2j} \\ \cos(\alpha) &= \frac{e^{j\alpha}+e^{-j\alpha}}{2j} \end{aligned} \tag{5}$$

The term sin(3θe + 2β) can be expanded using the trigonometric identity as:

$$\sin(3\theta_e + 2\beta) = \sin(3\theta_e)\cos(2\beta) + \cos(3\theta_e)\sin(2\beta) \tag{6}$$

Thus, the second term in Equation (3), which represents the torque ripple component, can be rewritten as:

$$T_{e_ripple} = \frac{3}{8} N_r L_\delta \left(i_d^2 + i_q^2\right) (\sin(3\theta_e)\cos(2\beta) + \cos(3\theta_e)\sin(2\beta)) \tag{7}$$

This form reflects that the ripple component has both sine and cosine terms due to the advanced current angle β. Physically, this means that depending on the value of β, the torque ripple will exhibit a phase shift that combines both sine and cosine components.

The angle β is related to the ratio between the d-axis and q-axis currents, which determines the phase shift in the current vector of the VFRM. Specifically, β can be calculated as:

$$\beta = \tan^{-1}\left(\frac{i_d^2}{i_q^2}\right) \tag{8}$$

when $i_d = 0$, $\beta = 0$, and the torque ripple component simplifies to a pure sine function $sin(3\theta_e)$ without any cosine component.

For non-zero i_d, β introduces a phase shift, causing both sine and cosine terms to appear in the torque ripple component.

Given this, we can write the final form of the torque ripple component as:

$$T_{e_ripple} = \frac{3}{8} N_r L_\delta \left(i_d^2 + i_q^2\right) \left(\sin(3\theta_e)\cos\left(2\tan^{-1}\left(\frac{i_d^2}{i_q^2}\right)\right) + \cos(3\theta_e)\sin\left(2\tan^{-1}\left(\frac{i_d^2}{i_q^2}\right)\right)\right) \tag{9}$$

This expression now accounts for both the sine and cosine components, with coefficients that depend on i_d and i_q through the advanced current angle β.

This decomposition shows that the torque ripple is a position-dependent periodic disturbance with both sine and cosine terms due to the phase shift β introduced by the d-axis current. The magnitude and phase of the ripple are influenced by the dq-axis currents, so it is possible to control the ripple by adjusting these currents.

3.2. Current Coupling Factors in VFRM

Equation (10) shows the voltage equation of the VFRM in a transient state.

$$\begin{cases} u_d = R_s i_d - \omega_e L_s i_q + L_s \frac{di_d}{dt} + L_\delta \frac{di_0}{dt} \\ u_q = R_s i_q + \omega_e L_s i_d + \omega_e L_\delta i_0 + L_s \frac{di_q}{dt} \\ u_0 = R_s i_0 + L_s \frac{di_0}{dt} + \frac{L_\delta}{2} \frac{di_d}{dt} \end{cases} \tag{10}$$

Figure 3 illustrates the block diagram of the VFRM and its current controller drawn according to Equation (10), where delays due to sampling and computational errors are ignored and G_c is the transfer function of the current controller; u_d*, u_q*, and u_0* are the reference voltages output from the d-axis, q-axis, and 0-axis current controllers, respectively. In the VFRM, there is a cross-coupling between the d-axis and the q-axis, a differential term coupling between the d-axis and the 0-axis, and a perturbation of the 0-axis to the q-axis. Therefore, the VFRM is a system containing complex inter-axis couplings.

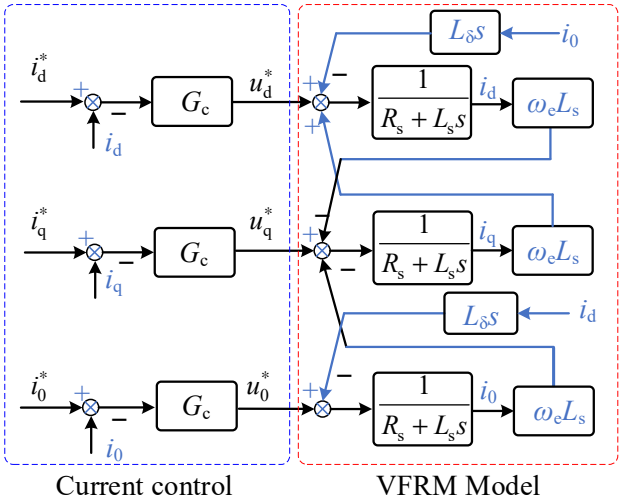

Figure 3. Block diagram of the VFRM and its current controller.

The differential term coupling is difficult to access directly, and there are other unknown perturbations in the system, such as inverter nonlinearities and motor parameter variations, which affect the effectiveness of feed-forward decoupling control. Therefore, in this paper, an ITHESO is used to observe the total current loop perturbations caused by factors such as coupling, perturbation terms, and a torque ripple component. The ITHESO requires little information about the system model and can perform state reconstruction for unknown nonlinear systems.

The input signals of the ITHESO are the d-axis, q-axis, and 0-axis reference voltages, while the voltage references include the inverter nonlinear voltages in addition to the actual voltages acting on the motor windings. During the operation of the motor, both the motor parameters and the inverter nonlinearities change, and these factors are considered as uncertain disturbances, denoted by d. Then the voltage equation can be expressed as:

$$\begin{cases} u_\mathrm{d} = R_\mathrm{s} i_\mathrm{d} + L_\mathrm{s} \frac{\mathrm{d}i_\mathrm{d}}{\mathrm{d}t} - \omega_\mathrm{e} L_\mathrm{s} i_\mathrm{q} + L_\delta \frac{\mathrm{d}i_0}{\mathrm{d}t} + d_\mathrm{d} \\ u_\mathrm{q} = R_\mathrm{s} i_\mathrm{q} + L_\mathrm{s} \frac{\mathrm{d}i_\mathrm{q}}{\mathrm{d}t} + \omega_\mathrm{e} L_\mathrm{s} i_\mathrm{d} + \omega_\mathrm{e} L_\delta i_0 + d_\mathrm{q} \\ u_0 = R_\mathrm{s} i_0 + L_\mathrm{s} \frac{\mathrm{d}i_0}{\mathrm{d}t} + L_\mathrm{s} \frac{\mathrm{d}i_0}{\mathrm{d}t} + \frac{L_\delta}{2} \frac{\mathrm{d}i_\mathrm{d}}{\mathrm{d}t} + d_0 \end{cases} \tag{11}$$

The transformation gives

$$\begin{cases} \frac{\mathrm{d}i_\mathrm{d}}{\mathrm{d}t} = \frac{u_\mathrm{d}}{L_\mathrm{s}} - \frac{R_\mathrm{s}}{L_\mathrm{s}} i_\mathrm{d} + \omega_\mathrm{e} i_\mathrm{q} - \frac{L_\delta}{L_\mathrm{s}} \frac{\mathrm{d}i_0}{\mathrm{d}t} - \frac{d_\mathrm{d}}{L_\mathrm{s}} \\ \frac{\mathrm{d}i_\mathrm{q}}{\mathrm{d}t} = \frac{u_\mathrm{q}}{L_\mathrm{s}} - \frac{R_\mathrm{s}}{L_\mathrm{s}} i_\mathrm{q} - \omega_\mathrm{e} i_\mathrm{d} - \omega_\mathrm{e} \frac{L_\delta}{L_\mathrm{s}} i_0 - \frac{d_\mathrm{q}}{L_\mathrm{s}} \\ \frac{\mathrm{d}i_0}{\mathrm{d}t} = \frac{u_0}{L_\mathrm{s}} - \frac{R_\mathrm{s}}{L_\mathrm{s}} i_0 - \frac{L_\delta}{2L_\mathrm{s}} \frac{\mathrm{d}i_\mathrm{d}}{\mathrm{d}t} - \frac{d_0}{L_\mathrm{s}} \end{cases} \tag{12}$$

where d_d, d_q, and d_0 denote the uncertainty perturbations caused by parameter variations and inverter nonlinearities in the dq0-axis current loops.

3.3. Design of Decoupled Current Control with ITHESO for Torque Ripple Reduction

According to the principle of ITHESO, the d-axis, q-axis, and 0-axis observers are designed for the current decoupling of VFRM while accounting for torque ripple disturbance, respectively. Equation (12) can be expressed as:

$$\begin{cases} \dot{i}_\mathrm{d} = f_\mathrm{d} + b_\mathrm{d} u_\mathrm{d} \\ \dot{i}_\mathrm{q} = f_\mathrm{q} + b_\mathrm{q} u_\mathrm{q} \\ \dot{i}_0 = f_\mathrm{q} + b_\mathrm{q} u_0 \end{cases} \tag{13}$$

where f_d, f_q, and f_0 are the total perturbations in each current loop and b_d, b_q, and b_0 are the feedback coefficients of each reference voltage. These two parameters can be expressed as shown in Equations (14) and (15), respectively. It should be noted that in the proposed design, parameter mismatches such as variations in inductance, are captured as part of the total disturbance (f_d, f_q, f_0). The ITHESO dynamically estimates and compensates for these disturbances, meaning the performance of the observer is less affected when L_s in Equation (15) changes with operating conditions.

$$\begin{cases} f_d = \frac{1}{L_s}\left(-R_s i_d + \omega_e L_s i_q - L_\delta \frac{di_0}{dt} - (d_d + T_{e_ripple})\right) \\ f_q = \frac{1}{L_s}\left(-R_s i_q - \omega_e L_s i_d - \omega_e L_\delta i_0 - (d_q + T_{e_ripple})\right) \\ f_0 = -\frac{1}{L_s}\left(R_s i_0 - \frac{L_\delta}{2}\frac{di_d}{dt} - (d_0 + T_{e_ripple})\right) \end{cases} \tag{14}$$

$$\left\{ b_d = b_q = b_0 = \frac{1}{L_s} \right. \tag{15}$$

According to Equation (13), the d, q, and 0-axis current loops are reconstructed as shown in (16), (17) and (18), respectively.

$$\begin{cases} \dot{i_d} = f_d + b_d u_d \\ f_d = w_d \\ y_d = i_d \end{cases} \tag{16}$$

$$\begin{cases} \dot{i_q} = f_q + b_q u_q \\ f_q = w_q \\ y_q = i_q \end{cases} \tag{17}$$

$$\begin{cases} \dot{i_0} = f_0 + b_0 u_0 \\ f_0 = w_0 \\ y_0 = i_0 \end{cases} \tag{18}$$

where y_d, y_q, y_0 are the outputs of the current loop and w_d, w_q, w_0 are bounded functions.

Therefore, the dq0-axis ITHESO observers for observing the coupling and disturbance terms in the VFRM are designed as

$$\begin{cases} e_d = \hat{i_d} - i_d \\ \dot{\hat{i_d}} = \hat{f_d} - \beta_{d1} e_d + b_d u_d \\ \dot{\hat{f}_d} = -\beta_{d2} e_d \end{cases} \tag{19}$$

$$\begin{cases} e_q = \hat{i_q} - i_q \\ \dot{\hat{i_q}} = \hat{f_q} - \beta_{q1} e_q + b_q u_q \\ \dot{\hat{f}_q} = -\beta_{q2} e_q \end{cases} \tag{20}$$

$$\begin{cases} e_0 = \hat{i_0} - i_0 \\ \dot{\hat{i_0}} = \hat{f_0} - \beta_{01} e_0 + b_0 u_0 \\ \dot{\hat{f}_0} = -\beta_{02} e_0 \end{cases} \tag{21}$$

where e_d, e_q, e_0 are the errors of the estimated and real currents in the ITHESO, respectively, and β_{d1}, β_{d2}, β_{q1}, β_{q2}, β_{01}, β_{02} are the gains of the errors, respectively.

Further, the expression of the control input can be organized according to (13) as

$$\begin{cases} u_{\mathrm{d}} + \frac{f_{\mathrm{d}}}{b_{\mathrm{d}}} = sL_{\mathrm{s}}i_{\mathrm{d}} \\ u_{\mathrm{q}} + \frac{f_{\mathrm{q}}}{b_{\mathrm{d}}} = sL_{\mathrm{s}}i_{\mathrm{q}} \\ u_0 + \frac{f_0}{b_{\mathrm{d}}} = sL_{\mathrm{s}}i_0 \end{cases} \tag{22}$$

where $\frac{f_{\mathrm{d}}}{b_{\mathrm{d}}}$, $\frac{f_{\mathrm{q}}}{b_{\mathrm{d}}}$, and $\frac{f_0}{b_{\mathrm{d}}}$ are the voltage disturbances of the dq0-axis current loops.

The block diagram of the VFRM decoupled current control based on the ITHESO is shown in Figure 4. The inputs to the ITHESO are the current feedback, the voltage reference, and position-dependent periodic disturbance to account for torque ripple. The output is the observed current feedback that takes the coupling factor and torque ripple factor into account. With the use of the ITHESO in the current control, the d, q, and 0-axis current loops are independent of each other, while the torque harmonic is dependent on all of the dq0-axis currents, and thus decoupling control and torque ripple reduction are realized simultaneously. From Equation (22), it can be seen that the VFRM model has been equated to an inductor at this point. According to the final value theorem, the steady-state error of the current loop includes a torque ripple component. Thus, a decoupled current controller is able to reduce the torque ripple.

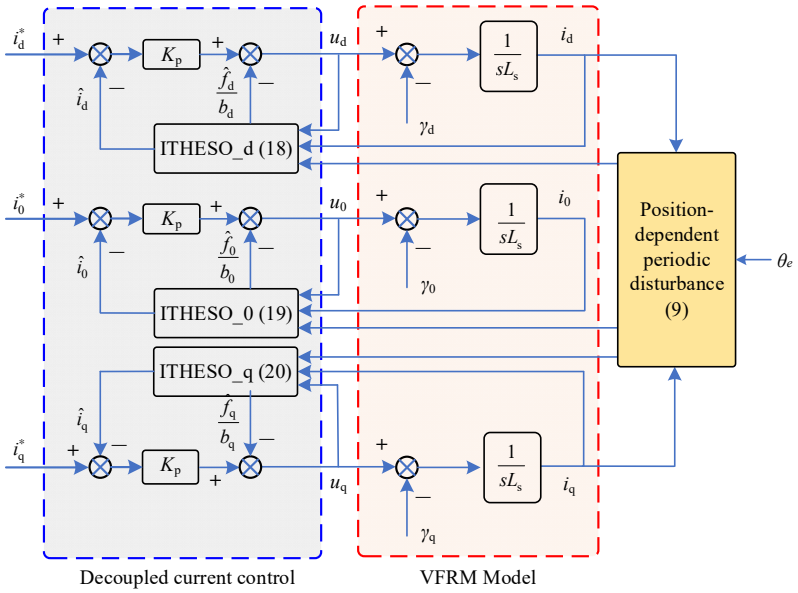

Figure 4. Diagram of decoupled current control based on ITHESO.

3.4. ITHESO Stability of the Decoupled Current Control

To confirm the stability of the decoupled current control for the VFRM system, a Lyapunov second theorem function for the closed loop system including the error dynamics of both the controller and the ITHESO should be established. The goal is to show that the Lyapunov function is positive definite and that its time derivative is negative semi-definite, indicating stability.

The decoupled current control includes dynamics for the dq0-axis currents with disturbances due to torque ripple, which can be defined as

$$\begin{aligned} e_d &= i_{\mathrm{d}} - i_{\mathrm{d}}^* \\ e_q &= i_{\mathrm{q}} - i_{\mathrm{q}}^* \\ e_0 &= i_0 - i_0^* \end{aligned} \tag{23}$$

For each axis, the ITHESO estimates current disturbances in the system, including position-dependent periodic disturbances.

A Lyapunov candidate function that includes terms for the current tracking errors and the ITHESO estimation errors is proposed. Let us define a composite Lyapunov function V as:

$$V = \frac{1}{2}e_d^2 + \frac{1}{2}e_q^2 + \frac{1}{2}e_0^2 \tag{24}$$

This function V is positive definite, as each component is positive when the errors are non-zero.

To ensure stability, the time derivative V should be negative semi-definite (or, ideally, negative definite). Taking the time derivative of V:

$$\dot{V} = e_d\dot{e_d} + e_q\dot{e_q} + e_0\dot{e_0} \tag{25}$$

from Equation (22), the current error dynamics are influenced by the control inputs and the disturbances. This assumes that the primary control laws are designed to stabilize the system in the absence of disturbances and the disturbance compensations aim to cancel the harmonic disturbances.

Therefore, the current error dynamics become:

$$\begin{aligned} \dot{e_d} &= -k_d e_d + (d_\mathrm{d} + T_{e_ripple}) \\ \dot{e_q} &= -k_q e_q + (d_q + T_{e_ripple}) \\ \dot{e_0} &= -k_0 e_0 + (d_0 + T_{e_ripple}) \end{aligned} \tag{26}$$

The estimation errors have dynamics based on the ITHESO gains. Thus, substituting Equation (26) into (25) yields

$$\begin{aligned} \dot{V} = \quad & e_d(-k_d e_d + (d_\mathrm{d} + T_{e_ripple})) + e_q(-k_q e_q + (d_q + T_{e_ripple})) \\ & + e_0(-k_0 e_0 + (d_0 + T_{e_ripple})) \end{aligned} \tag{27}$$

Rearranging terms, this becomes

$$\begin{aligned} \dot{V} = \quad & -k_d e_d^2 - k_q e_q^2 - k_0 e_0^2 + e_d(d_\mathrm{d} + T_{e_ripple}) \\ & + e_q(d_q + T_{e_ripple}) + e_0(d_0 + T_{e_ripple}) \end{aligned} \tag{28}$$

The ITHESO effectively estimates and compensates for disturbances and torque ripple components. Assuming that the disturbance estimation error is bounded and can be reduced to negligible levels through proper observer design, the disturbance terms can be approximated as:

$$(d_\mathrm{d} + T_{e_ripple}) \approx 0,\ (d_q + T_{e_ripple}) \approx 0,\ (d_0 + T_{e_ripple}) \approx 0 \tag{29}$$

Thus, $\dot{V}$ simplifies to:

$$\dot{V} = -k_d e_d^2 - k_q e_q^2 - k_0 e_0^2 \tag{30}$$

Since k_d, k_q, and $k_0 > 0$, all of the terms in Equation (30) are negative or zero. This implies:

$$\dot{V} \leq 0 \tag{31}$$

Since V is positive definite and $\dot{V}$ is negative semi-definite, the equilibrium point (where $e_\mathrm{d} = e_\mathrm{q} = e_0 = 0$) is stable.

3.5. Overall Decoupled Current Control Based ITHESO

The illustrated diagram of the all-encompassing control strategy that incorporates decoupled current control via ITHESO is depicted in Figure 5. This setup incorporates three current loops and a singular speed loop. To enhance torque efficiency and curtail copper losses, the paper employs the MTPA control methodology. In this arrangement, the opposing U_0 voltage is modulated through the i_0 current produced by the dual inverter. After determining the current disturbances using the proposed ITHESO observer, the proposed decoupled current control initiates the process of rejecting disturbances while reducing the torque ripple. The main purpose of this method is to combine the position-dependent periodic disturbance with current disturbances for effective torque ripple reduction. The results produced from the ITHESO observers are fed back to be compared with the dq0-axis current references through a proportional term, thereby facilitating the concurrent regulation of the current control loops.

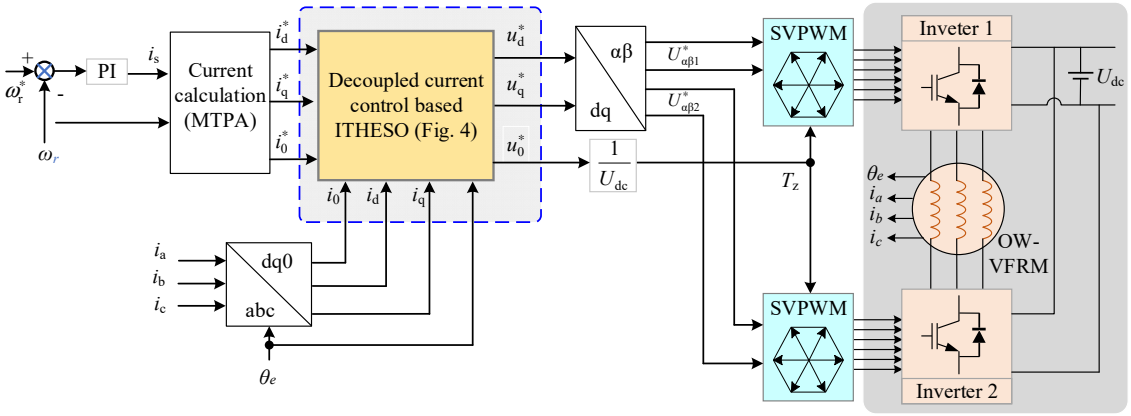

Figure 5. Diagram of the decoupled current control system based on ITHESO.

4. Experimental Results

A dual-inverter configuration was employed for an open winding 6/4 VFRM (State Key Laboratory of Reliability and Intelligence of Electrical Equipment, Hebei University of Technology, Tianjin, China) to assess the effectiveness of the decoupled current control-based ITHESO in rejecting disturbances and reducing torque ripple. The setup included the particular specifications of the VFRM as outlined in Table 1, while a schematic representation of the experimental apparatus is presented in Figure 6. The operation of the VFRM was governed by a dual-inverter system, with control performed via a dSPACE 1202 connected to MATLAB 2015a, and the IGBT switching frequency was maintained at 10 kHz. The load for the experimental validation was provided by a dynamometer with a rated torque of 7.5 Nm, a power range of 750 W to 1500 W, and a maximum speed of 5000 rpm. This setup enabled realistic testing conditions, replicating dynamic torque and speed variations to evaluate the proposed control strategy. The analysis of the torque output from the VFRM was conducted utilizing a Kistler 4502A torque sensor in conjunction with a Yokogawa DL850E, which served as the oscilloscope for the experimental procedures.

During the experimental procedures, the torque ripple of the VFRM, as assessed, is defined by ΔT_{ripple}, which is derived by deducting the minimum torque from the maximum torque and subsequently normalizing this difference using the average torque, as specified in (32). Simultaneously, the voltage utilization amplitude U_s is computed by taking the

square root of the total of the squares of the dq-axis voltages complemented by the zero-sequence voltage, as described in (33).

$$\Delta T_{ripple} = \frac{T_{e_\max} - T_{e_\min}}{T_{e_avg}} \tag{32}$$

$$|U_s| = \sqrt{U_d^2 + U_q^2} + U_0 \tag{33}$$

Table 1. VFRM Parameters.

Parameters	Value and Unit	Parameters	Value and Unit
Stator outer diameter	90 mm	Number of phases	3
Rotor outer diameter	46.4 mm	Rated torque	0.4
Axial length	25 mm	Poles of stator	6
Air gap	0.5 mm	Phase resistance	3 Ω
Turns per phase	366	AC component of stator inductance (Ls)	30 mH
Current density	5.8 A/mm^2	DC component of stator inductance (Lδ)	24 mH

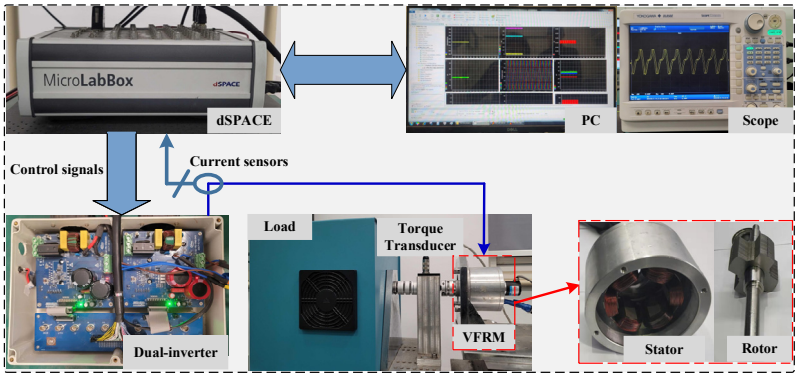

Figure 6. Experimental setups.

The first experiment compares the steady-state performance of the proposed decoupled current control with conventional ADRC control, taking into account torque disturbances. As can be seen in Figure 7, the conventional method has a torque ripple of 0.08 Nm. The proposed method reduces the torque ripple to 0.02 Nm. Evidently, the torque ripple reduction using the proposed method is due to the accurate modeling and proper design of the decoupled current controller.

In terms of phase currents, i_{abc} in both methods are sinusoidal, indicating high stability. The i_{dq0} are smoother under both methods, demonstrating better decoupling and disturbance rejection. Additionally, the DC link voltage utilization U_s is more efficient and less distorted with decoupled current control, reflecting improved power quality and better system performance. Overall, decoupled current control offers superior performance by minimizing torque ripple and voltage fluctuations while enhancing DC link utilization, making it more effective for VFRM operation.

When the speed is 900 rpm and the load is set to 0.17 Nm, the FFT analysis results of the phase current are shown in Figure 8. When implementing the proposed method, the current component of the 2nd harmonic decreases from 7.15% to 6.88%, the current component of the 3rd harmonic increases from 1.02% to 15.77% and the current component of the 4th harmonic decreases from 1.08% to 0.29%. Note that the proposed current control scheme is not aimed at eliminating specific harmonic currents, but at reducing the torque ripple, taking into account the dq0-axis current coupling. The presence of higher-order

harmonic current components is necessary because the fundamental current interacts with itself to generate the main torque ripple. In the proposed method, the remaining third harmonic current interacts with itself to offset the inherent torque ripple caused by the fundamental current, which can be verified experimentally.

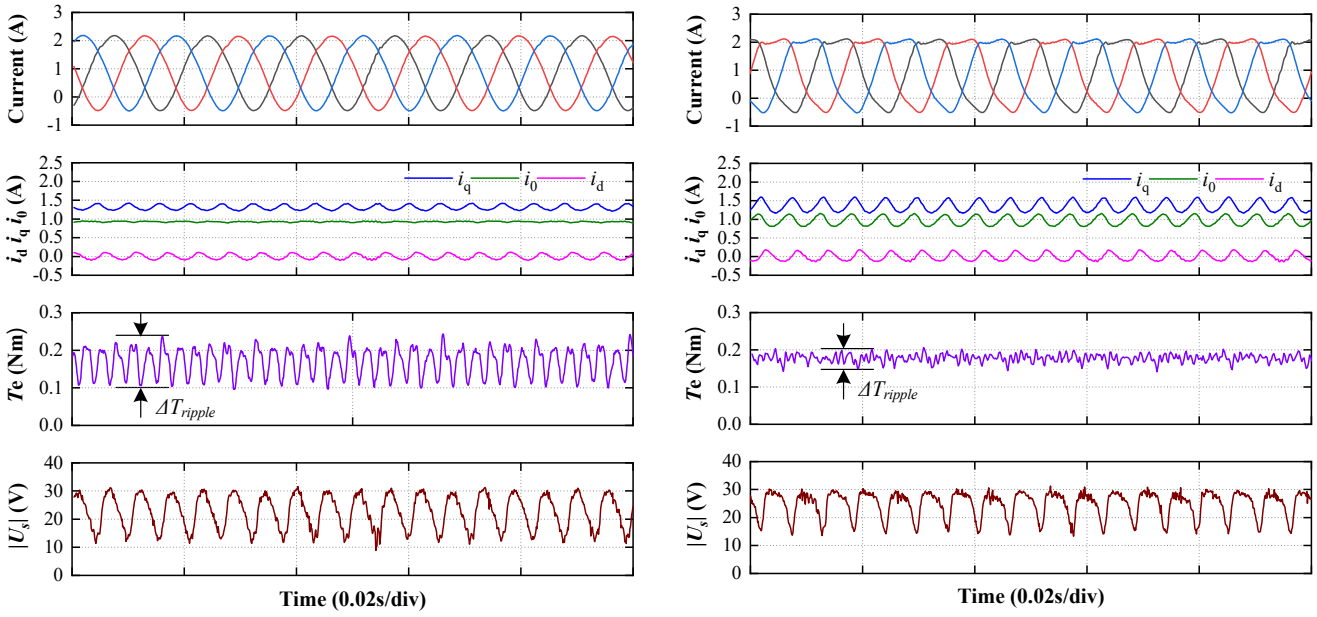

Figure 7. Comparison of steady-state waveforms at a speed of 900 rpm with a load configured to 0.17 Nm: (**a**) ADRC. (**b**) Decoupled Current Control.

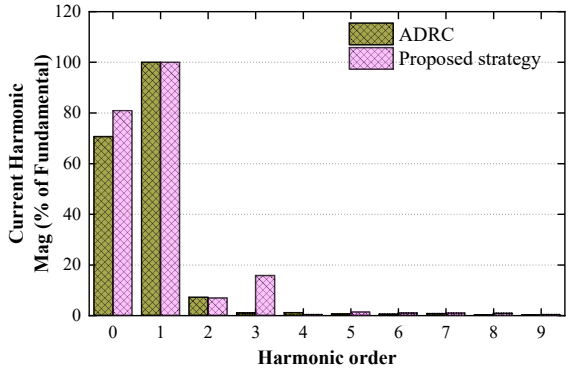

Figure 8. Comparison of FFT analysis results of phase current when the speed is 900 rpm and the load is configured to 0.17 Nm.

Figure 9 compares the transient responses of torque under ADRC and the proposed strategy, as demonstrated in the second experiment. Figure 9a,b shows the torque result when the speed increases from 600 rpm to 900 rpm. Figure 10a,b illustrates the system's behavior during a speed reduction from 900 rpm to 600 rpm. The analysis of these plots reveals the distinct advantages of the proposed strategy in terms of torque ripple reduction.

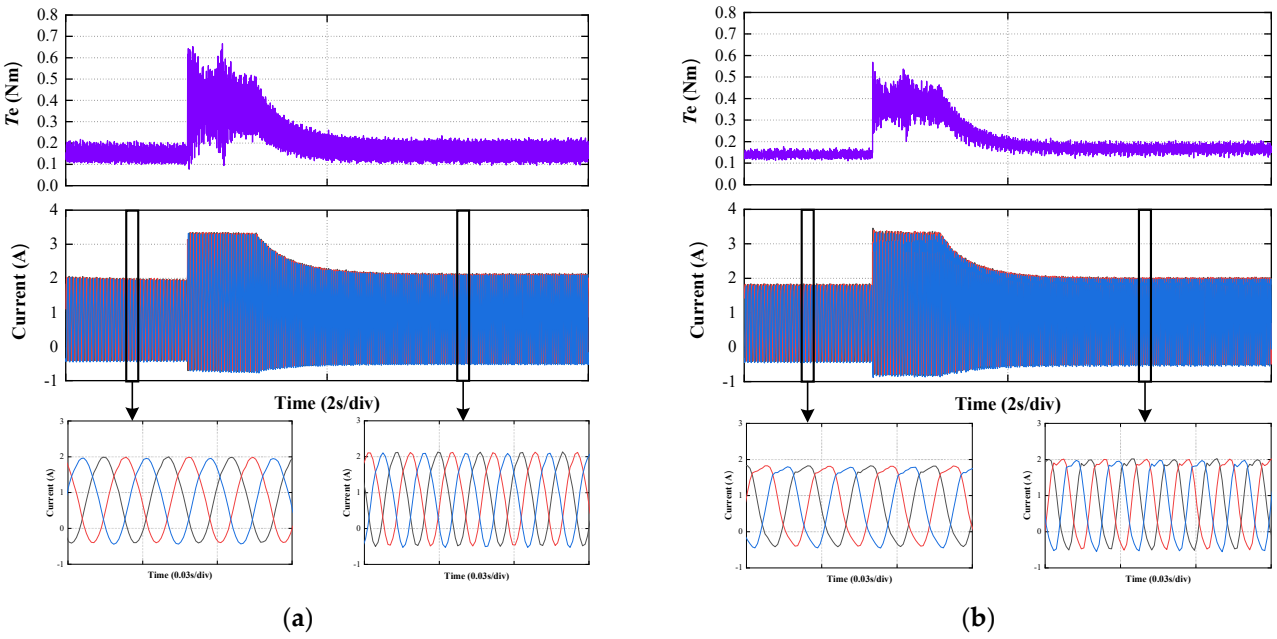

Figure 9. Comparison of transient state waveforms with a load configured to 0.17 Nm and an increase in speed from 600 rpm to 900 rpm. (**a**) ADRC. (**b**) Proposed strategy.

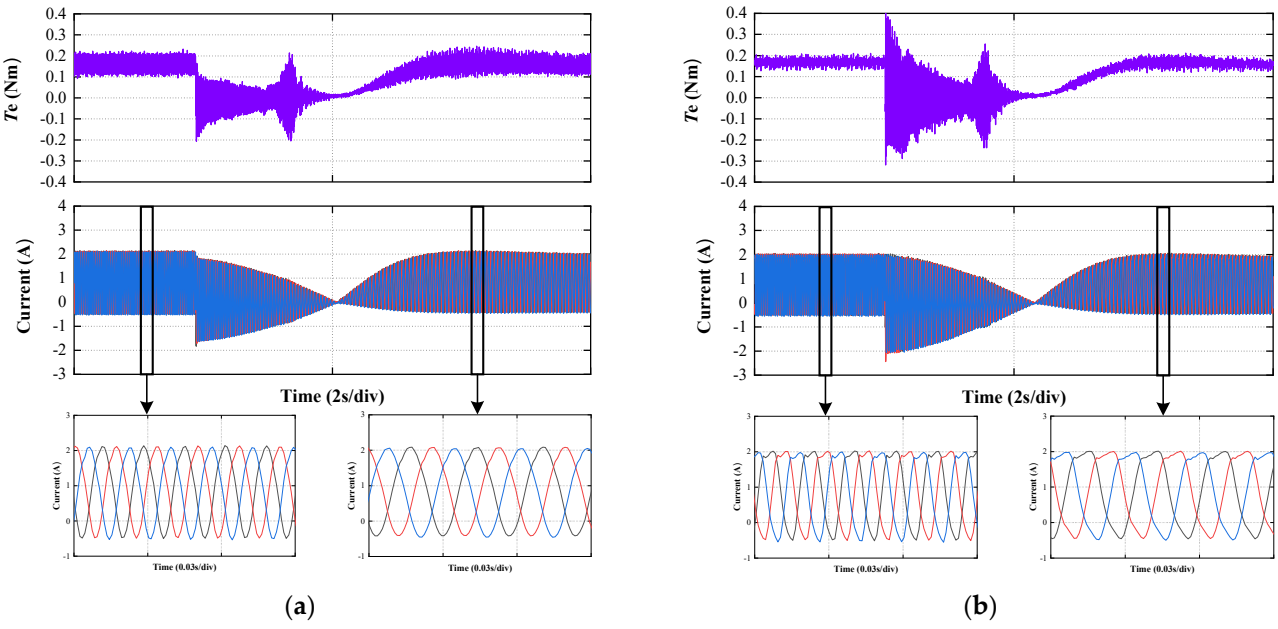

Figure 10. Comparison of transient state waveforms with a load configured to 0.17 Nm and decrease in speed from 900 rpm to 600 rpm. (**a**) ADRC. (**b**) Proposed strategy.

In terms of overshoot, the proposed strategy exhibits a clear advantage over ADRC. During both speed transitions, ADRC displays a significant overshoot, with torque peaking further from the desired value. In Figure 9, where the speed increases, ADRC overshoots notably, whereas the proposed method maintains the torque closer to the target. Similarly, in Figure 10, during the speed decrease, the ADRC control shows a pronounced overshoot, while the proposed strategy responds more smoothly. This reduction in overshoot with the proposed method indicates improved control over sudden torque changes, which is beneficial for minimizing mechanical stress on the machine.

The proposed strategy also outperforms ADRC in terms of settling time. Across both speed changes, the torque under the proposed method reaches a stable state more quickly than with ADRC. This faster settling time suggests that the proposed strategy adapts more

effectively to the new speed commands and has better disturbance rejection capabilities. By stabilizing the torque faster, the proposed strategy ensures a more responsive system, which is advantageous for applications that require rapid adjustments.

Figure 11 compares the performance of the proposed control strategy under precise machine parameters (before the red line) and with a −30% deviation in self-inductance (after the red line). The electromagnetic torque remains stable and exhibits minimal ripple even under parameter uncertainties, demonstrating effective torque regulation.

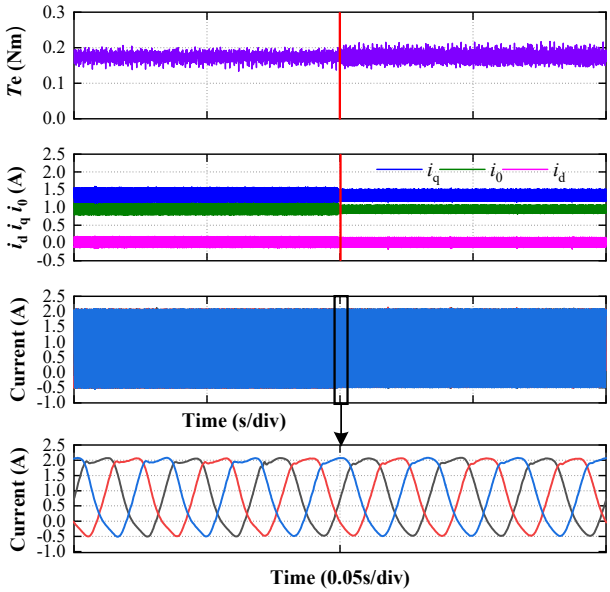

Figure 11. Comparative experimentation amidst parameter uncertainties. Proposed strategy utilizing precise parameters (before red line). Proposed strategy incorporating parameter uncertainties (after redline).

The decoupled currents idq0 are well-regulated, while slight variations appear after the red line, the control strategy effectively mitigates disturbances and maintains steady decoupling. Similarly, the phase currents i_{abc} remain sinusoidal and balanced, reflecting robust current regulation despite parameter deviations. The proposed strategy ensures stable performance under significant uncertainties, making it suitable for practical applications in which machine parameters can vary due to manufacturing tolerances or operating conditions. Its robustness enhances the reliability and performance of VFRM. Furthermore, while the ITHESO demonstrates robustness to parameter mismatches, its performance could degrade under extreme parameter variations or unmodeled nonlinearities. Fine-tuning the observer gains is necessary to maintain optimal performance across all operating conditions.

Overall, these improvements make the proposed method particularly advantageous for EV applications. Torque ripple reduction minimizes mechanical vibrations and noise, leading to improved passenger comfort and quieter operation. The method's robustness to parameter mismatches and external disturbances ensures reliable performance under varying speeds and loads, which are common in EV drive cycles.

5. Conclusions

This paper presents a decoupled current control based ITHESO for reducing torque ripple in open winding VFRMs. In order to explain the relationship between position-dependent torque ripple and current loop disturbance, a comprehensive analysis is carried out. In contrast to the conventional ADRC method, the torque component responsible for the torque ripple is integrated into a decoupled current control using the proposed ITHESO

observer. This eliminates the torque ripple during steady and transient states and improves the performance of the VFRM.

The presented method has several advantages: First, by integrating the torque component in the decoupled current control using the ITHESO, the torque ripple is reduced by more than 50%. Second, the proposed method is mostly independent of the VFRM parameters, which makes it robust to parameter uncertainties. Finally, the efficiency and positive aspects of the proposed method are supported by experimental results, which show that the torque ripple reduction is feasible under both transient load and speed variation conditions, while maintaining the DC link voltage at a minimum amplitude, thus improving the overall effectiveness of the DC link voltage. Future work could explore extending the proposed framework to address higher-order harmonics, adapt the strategy for multi-phase systems and other machine topologies, and further optimize computational efficiency for broader applicability in real-time control systems.

Author Contributions: Conceptualization, E.M.A., X.L. and A.A.; Methodology, E.M.A. and X.L.; Software, E.M.A.; Validation, E.M.A. and X.L.; Formal analysis, E.M.A., X.L., M.A.H. and A.A.; Investigation, E.M.A.; Resources, X.L., A.A., M.A.H., J.A.K., Y.C. and M.E.A.; Data curation, E.M.A. and X.L.; Writing—original draft, E.M.A.; Writing—review and editing, E.M.A., X.L., A.A. and Y.C.; Visualization, E.M.A., X.L. and J.A.K.; Supervision, X.L.; Funding acquisition, X.L. All authors have read and agreed to the published version of the manuscript.

Funding: This work was supported by the Natural Science Foundation of China under Grant 52077055; Projects of Central Government to Guide Local Scientific and Technological Development under Grant 226Z1601G; Tianjin Science and Technology Projects: 22JCZDJC00950.

Data Availability Statement: The original contributions presented in the study are included in the article, further inquiries can be directed to the corresponding authors.

Conflicts of Interest: The authors declare no conflicts of interest.

References

1. Liu, X.; Zhu, Z.Q. Comparative study of novel variable flux reluctance machines with doubly fed doubly salient machines. *IEEE Trans. Magn.* **2013**, *49*, 3838–3841. [CrossRef]
2. Liu, X.; Zhu, Z.Q. Electromagnetic performance of novel variable flux reluctance machines with dc-field coil in stator. *IEEE Trans. Magn.* **2013**, *49*, 3020–3028. [CrossRef]
3. Fukami, T.; Matsuura, Y.; Shima, K.; Momiyama, M.; Kawamura, M. A multipole synchronous machine with nonoverlapping concentrated armature and field windings on the stator. *IEEE Trans. Ind. Electron.* **2012**, *59*, 2583–2591. [CrossRef]
4. Hu, W.; Ruan, C.; Nian, H.; Sun, D. Simplified modulation scheme for open-end winding PMSM system with common DC link under open phase fault based on circulating current suppression. *IEEE Trans. Power Electron.* **2020**, *35*, 10–14. [CrossRef]
5. Baiju, M.R.; Mohapatra, K.K.; Kanchan, R.S.; Gopakumar, K. A dual two-level inverter scheme with common mode voltage elimination for an induction motor drive. *IEEE Trans. Power Electron.* **2004**, *19*, 794–805. [CrossRef]
6. Jahns, T.M.; Soong, W.L. Pulsating torque minimization techniques for permanent magnet ac motor drives—A review. *IEEE Trans. Ind. Electron.* **1996**, *43*, 321–330. [CrossRef]
7. Cui, Y.; Zhang, F.; Huang, L.; Chen, Z. Analysis and verification of a cogging torque reduction method for variable flux memory permanent magnet machine. *Electronics* **2021**, *10*, 1913. [CrossRef]
8. Husain, T.; Hasan, I.; Sozer, Y.; Husain, I.; Muljadi, E. Cogging torque minimization in transverse flux machines. *IEEE Trans. Ind. Appl.* **2019**, *55*, 385–397. [CrossRef]
9. Yang, Y.; Bianchi, N.; Bramerdorfer, G.; Zhang, C.; Zhang, S. Methods to improve the cogging torque robustness under manufacturing tolerances for the permanent magnet synchronous machine. *IEEE Trans. Energy Convers.* **2021**, *36*, 2152–2162. [CrossRef]
10. Nakao, N.; Akatsu, K. Suppressing pulsating torques: Torque ripple control for synchronous motors. *IEEE Ind. Appl. Mag.* **2014**, *20*, 33–44. [CrossRef]
11. Wang, T.; Luo, G.; Cheng, Y.; Tu, W.; Liu, C.; Chen, Z. Robust Finite-Control-Set Model Predictive Torque Control of PMSM Drives Based on Dual Variable Bandwidth ESOs. *IEEE Trans. Transp. Electrif.* **2024**, *10*, 8443–8456. [CrossRef]

12. Zmood, D.N.; Holmes, D.G. Stationary frame current regulation of PWM inverters with zero steady-state error. *IEEE Trans. Power Electron.* **2003**, *18*, 814–822. [CrossRef]
13. Rowan, T.M.; Kerkman, R.J. A new synchronous current regulator and an analysis of current-regulated PWM inverters. *IEEE Trans. Ind. Appl.* **1986**, *IA-22*, 678–690.
14. Xia, C.; Ji, B.; Yan, Y. Smooth speed control for low-speed high-torque permanent-magnet synchronous motor using proportional–integral-resonant controller. *IEEE Trans. Ind. Electron.* **2015**, *62*, 2123–2134. [CrossRef]
15. Yuan, X.; Merk, W.; Stemmler, H.; Allmeling, J. Stationary-frame generalized integrators for current control of active power filters with zero steady-state error for current harmonics of concern under unbalanced and distorted operating conditions. *IEEE Trans. Ind. Appl.* **2002**, *38*, 523–532. [CrossRef]
16. Mirkin, L. On dead-time compensation in repetitive control. *IEEE Control Syst. Lett.* **2020**, *4*, 791–796. [CrossRef]
17. Liu, X.; Aouiche, E.M.; Aouiche, A.; Cao, Y.; Aguida, M.E. Torque Ripple Suppression in the 6/4 Variable Flux Reluctance Machine with Open Winding Configuration by Using Harmonic Injection. *Energies* **2024**, *17*, 2753. [CrossRef]
18. Zuo, Y.; Zhu, J.; Yuan, X.; Lee, C.H. Two-degree-of-freedom quasi-pir controller for smooth speed control of permanent magnet vernier machine. In Proceedings of the 2021 IEEE Energy Conversion Congress and Exposition (ECCE), Vancouver, BC, Canada, 10–14 October 2021; pp. 5022–5028.
19. Hu, M.; Hua, W.; Ma, G.; Xu, S.; Zeng, W. Improved current dynamics of proportional-integral-resonant controller for a dual three-phase FSPM machine. *IEEE Trans. Ind. Electron.* **2021**, *68*, 11719–11730. [CrossRef]
20. Gao, Z. On the centrality of disturbance rejection in automatic control. *ISA Trans.* **2014**, *53*, 850–857. [CrossRef] [PubMed]
21. Zuo, Y.; Zhu, X.; Quan, L.; Zhang, C.; Du, Y.; Xiang, Z. Active disturbance rejection controller for speed control of electrical drives using phase-locking loop observer. *IEEE Trans. Ind. Electron.* **2019**, *66*, 1748–1759. [CrossRef]
22. Zuo, Y.; Chen, J.; Zhu, X.; Lee, C.H. Different active disturbance rejection controllers based on the same order GPI observer. *IEEE Trans. Ind. Electron.* **2022**, *69*, 10969–10983. [CrossRef]
23. Chen, P.; Luo, Y.; Zhang, L.; Wang, X.; Chen, Y. PMSM Speed Ripple Suppression Due to Current Measurement Error Using Quasi-Fractional Resonant-Normalized Extended State Observer. *IEEE Trans. Control Syst. Technol.* **2024**. [CrossRef]
24. Song, Z.; Wang, Y.; Shi, T. A dual-loop predictive control structure for permanent magnet synchronous machines with enhanced attenuation of periodic disturbances. *IEEE Trans. Power Electron.* **2020**, *35*, 760–774. [CrossRef]
25. Chen, W.-H. Disturbance observer-based control for nonlinear systems. *IEEE/ASME Trans. Mechatron.* **2004**, *9*, 706–710. [CrossRef]
26. Guo, B.; Bacha, S.; Alamir, M.; Hably, A.; Boudinet, C. Generalized integrator-extended state observer with applications to grid-connected converters in the presence of disturbances. *IEEE Trans. Control Syst. Technol.* **2021**, *29*, 744–755. [CrossRef]
27. Yang, X.; Hu, H.; Hu, H.; Liu, Y.; He, Z. A quasi-resonant extended state observer-based predictive current control strategy for three-phase PWM rectifier. *IEEE Trans. Ind. Electron.* **2022**, *69*, 13910–13917. [CrossRef]
28. Hu, M.; Hua, W.; Wang, Z.; Li, S.; Wang, P.; Wang, Y. Selective periodic disturbance elimination using extended harmonic state observer for smooth speed control in PMSM drives. *IEEE Trans. Power Electron.* **2022**, *37*, 13288–13298. [CrossRef]
29. Zhu, Z.Q.; Lee, B.; Liu, X. Integrated field and armature current control strategy for variable flux reluctance machine using open winding. *IEEE Trans. Ind. Appl.* **2016**, *52*, 1519–1529.

Disclaimer/Publisher's Note: The statements, opinions and data contained in all publications are solely those of the individual author(s) and contributor(s) and not of MDPI and/or the editor(s). MDPI and/or the editor(s) disclaim responsibility for any injury to people or property resulting from any ideas, methods, instructions or products referred to in the content.